ICRF Antenna Operation with Full W-wall in ASDEX Upgrade

V. Bobkov 1), F. Braun 1), R. Dux 1), A. Herrmann 1), L. Giannone 1), A. Kallenbach 1), H.W. Müller 1), R. Neu 1), J.-M. Noterdaeme 1) 2), T. Pütterich 1), V. Rohde 1), A. Sips 1), A. Krivska 3) 4), I. Zammuto 1) and ASDEX Upgrade Team

1) Max-Planck-Institut für Plasmaphysik, EURATOM Association, Garching, GERMANY
2) Ghent University, EESA Department, Gent, Belgium
3) Institute of Plasma Physics ASCR, Euratom Association, Prague, Czech Republic
4) Czech Technical University of Prague, Telecommunication Engineering Department
e-mail: Volodymyr.Bobkov@ipp.mpg.de

Abstract. The compatibility of ICRF (Ion Cyclotron Range of Frequencies) antenna operation with high-Z plasma facing components (PFCs), needs improvement to keep ICRF as a good candidate for heating and current drive system in a fusion reactor. ASDEX Upgrade (AUG) with its tungsten (W) first wall and ICRF system allows to study ways to do this. A noticeable improvement of the ICRF operation with W-wall can be achieved by forcing low plasma temperature conditions at the PFCs. These conditions can be fulfilled by increasing plasma-antenna clearance and by strong gas puffing, thus approaching the conditions ITER ICRF antenna plans to operate at. W sputtering during ICRF can be significantly decreased when the intrinsic light impurity content is decreased. However, an additional improvement is required for further reduction of the high-Z impurity sputtering during ICRF in the present and for the future devices. The improved theoretical modelling of ICRF antenna near-fields shows that the RF voltages along the magnetic field lines may originate from RF currents on the antenna box to a large extent, and not directly from antenna straps and their RF magnetic flux. Experimental results in AUG corroborating this picture are described. The calculations for future antenna design show that a reduction of the antenna box contribution can be achieved by extending the antenna box parallel to the magnetic field and increasing the number of toroidally distributed straps with $(0\pi...\pi0)$ or $(0\pi...0\pi)$ phasing.

1. Introduction

Until now, experiments in many devices have shown that the use of the power applied by ICRF antennas in a machine with high-Z first wall materials or coatings does not allow to achieve the best performance as with low-Z first wall (see e.g. [1]). This is the consequence of increased sputtering rates due to elevated sheath voltages caused by ICRF. This appears usually not to be critical for low-Z materials, but can lead to a large radiation for high-Z materials. However, high-Z wall materials such as tungsten (W) could be more relevant for the future devices [2–4]. ASDEX Upgrade with its W first wall allows to study ways to improve the compatibility of ICRF with high-Z plasma facing components. The 2007 and the first half of the 2008 AUG experimental campaigns were conducted without a single boronisation [5,6], followed by several boronizations in the second half of the 2008 campaign.

There are two basic approaches for reduction of the W release during ICRF. One is based on operational optimization; and one is based on new antenna design with reduced parallel near-fields $E_{||}$ ($E_{||}$ contribute most to the elevated sheath voltages). This paper discusses the operational approach and gives a detailed outlook on the possible improvements of the antenna design.

2. Characterization of W release during ICRF in AUG

AUG uses standard H-minority resonance heating with 4 ICRF antennas, two straps each with $(0,\pi)$ phasing of the strap currents. The antenna connections include 3 dB-hybrid systems which isolate the RF transmitters from the antenna load. In this configuration two antennas operate simultaneously (antennas 1 and 2 form a pair as well as antennas 3 and 4, see the left hand side of Fig. 1). The phasing is thus fixed to $(0,\pi)$,$(\pi/2,3\pi/2)$ for the pairs. For a limited time during the experimental period, the 3dB-hybrids were bypassed and antennas 3 and 4 were connected independently, each to its own RF transmitter. This was done to operate these antennas in different time windows without mutual influence. Such operation is usually limited to L-mode discharges to avoid problems with antenna load tolerance of ICRF system in H-modes.

For the characterization of the mechanisms involved in the release of impurities during ICRF power input, AUG has a comprehensive set of diagnostics. Some of the antenna 4 limiters are connected to the antenna frame via shunts which provide measurements of the rectified current I_{DC} flowing through the limiters. Langmuir probes implemented in one of the guard limiters, far from antennas, but connected to antenna pair 12 along magnetic field lines, provide measurements of the floating potential V_{fl}. As an important diagnostics, spectroscopic monitoring is used for limiters on antennas 3 and 4. The viewing geometry is shown in Fig. 1. There are eight poloidally distributes lines of sight for antenna 3 and five for antenna 4. Measured tungsten W and hydrogen D(H) line intensities are linked directly to the particle fluxes (Γ_W and Γ_D correspondingly) at the points of observation [7]. Effective sputtering yields Y_W are calculated by dividing Γ_W by Γ_D measured on the same line of sight [7]. Values of Y_W are therefore independent of the absolute error of Γ measurements. For a given content of the light impurities (concentrations and charge states), Y_W can be translated to a rectified sheath potential drop and theoretically to RF voltage $V_{||}$. The RF voltage $V_{||}$ can be calculated by integration of $E_{||}$ [8] along the magnetic field lines which are connected to the limiter. The W content in the plasma is characterized by the W concentration C_W measured at an electron temperature of ≈1.5 keV. For the discharges presented in this paper, this corresponds to the values of the poloidal radius between 0.4 and 0.9.

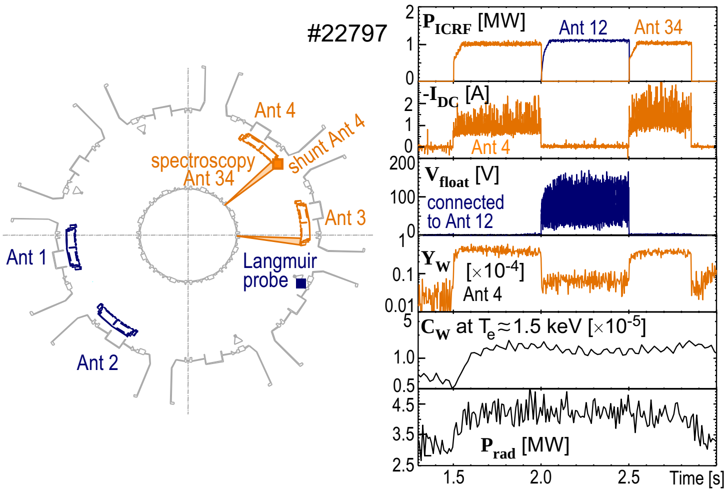

FIG. 1: Left: Locations of antennas and diagnostics in the torus. Right: Characterization of the W release during ICRF power input consequently from antenna pairs 12 and 34.

By following Fig. 1 from the top to the bottom, the mechanisms leading to the W release during ICRF can be described stepwise. Application of ICRF power (consequently antennas pairs 12 and 34) leads to an appearance of parallel electric fields $E_{||}$. Electrons are more mobile than ions and follow the fields fast and are lost on the limiters. The electron loss is registered by high negative values of I_{DC} measured on the antenna 4 limiter shunt. The loss of electrons leads to an increase of the plasma potential on the magnetic field lines with RF voltage $V_{||}$. The increase of plasma potential is observed by an increase of V_{fl} measured by the Langmuir probe connected to the antenna pair 12 when these antennas are active.

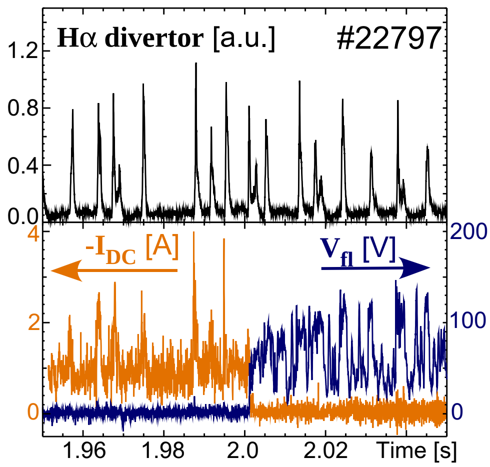

FIG. 2: Time-resolved measurements of I_{DC} at antenna 4 limiter and V_{fl} at the guard limiter (antenna pair 12). Power from antenna pair 34 is replaced by pair 12 at 2 sec.

Fig. 2 shows ELM-resolved measurements of I_{DC} and V_{fl} together with H_α in divertor which characterizes ELM activity. I_{DC} is the difference between electron and ion currents. In the high density case (no capacitive sheaths, which should apply here), the electron current represents the transient amount of electrons which has to be lost from a magnetic flux tube until a positive plasma potential has developed sufficient to equalize electron and ion losses. On average, this transient electron current is larger than ion saturation current, but smaller than electron saturation current. At a constant RF voltage on the field line $V_{||}$, the electron current is a measure of the external particle flux source, i. e. of the particle transport perpendicular to the magnetic field lines. This can be seen on the I_{DC} signal, which is the average of the transient electron current minus the ion current. The signal follows the density perturbations attributed to ELM activity. The V_{fl} time trace which approximately represents plasma potential (neglecting the electron temperature influence), also shows some correlation with ELM activity, but includes some other fluctuations not found on the H_α signal. The reason for this can be an additional perpendicular convection in the near-fields of the antenna.

The high positive plasma potential leads to an acceleration of light-impurity ions towards the PFCs. This causes the W sputtering. Significantly increased effective sputtering yields Y_W are measured spectroscopically at antenna 4 and are shown in Fig. 1 below the measurements of V_{fl}. The W sputtering leads to a large increase of the tungsten concentration when ICRF is on. In the case shown in Fig.1, the increment of total radiated power after the switching ICRF on approximately equals to the amount of ICRF power coupled ($\approx$ 1MW). Therefore it is important to study in which cases operation allows for lower W sputtering due to ICRF.

3. Operational ways to reduce ICRF induced sputtering

One of the ways to suppress the W release during ICRF is to use the plasma configurations with smaller outermost position of the plasma R_{out}. In other words, the plasma is shifted away from the antennas. Fig. 3 shows two discharges with different R_{out} values. Otherwise the discharges are identical. The discharge with lower R_{out} has lower local sputtering yield on the antenna limiters and lower W concentration. In the majority of these discharges, the first limiting surface is the central column, and the vessel components on the low field side are effectively in the shadow of the central column. Though the W source can be large on the central column, especially on the field lines connected to active ICRF antennas, it is observed [6] that penetration of W from the central column to the confined plasma is less efficient than that from the outer limiters. Therefore an increased W sputtering at the central column is less critical for the W concentration in the plasma.

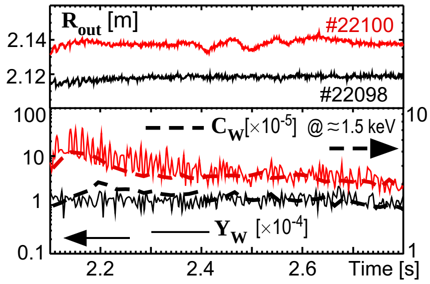

FIG. 3: Comparison of two discharges with different R_{out}, otherwise identical.

Another way to reduce the W release due to ICRF is by increasing the gas puffing rate. This works both for L- and H-modes, therefore it is not directly connected to the effect of the ELM frequency [6]. Fig. 4 illustrates the fact that sputtering yields and W concentration are lower at higher gas puff. The figure shows two similar discharges, one without boronization and one long after boronizations.

For the empirical findings on R_{out} and gas puff dependencies, the plasma temperature at PFCs is likely an important player. At large separatrix-antenna clearance, the density at the PFCs decreases while at high gas puff rate the density increases. RF near-fields are expected to increase in the first case and to decrease in the second case. Therefore it is very probable that the plasma temperature, lower in both cases, is the crucial parameter which leads to the reduction of the W source. Apart from the direct effect on the sheath potentials, an increase in the plasma temperature leads to an increase of the concentrations and the charge states of the background light impurities which sputter W. This plasma temperature dependence points out that an RF induced local plasma temperature increase can also contribute to W sputtering via

the influence on light impurities.
In the list of the light intrinsic impurities, oxygen (O) is one of the elements which had an increased concentration in the 2007/ early 2008 campaigns when no boronization was performed. The level of O can be efficiently reduced by O-gettering via boronization. The effect of decreased O level on sputtering in two very similar discharges (#23057 and #23517) is shown in Fig. 4, whereas the shot-to-shot evolution of O concentration is seen in Fig. 5 with the two shots highlighted. Shot #23517 was conducted sufficiently long after boronization (113 shots) to ensure there are no boron layers on antenna limiters anymore [9]. By the use of reduced NBI power of 5 MW in #23517 compared to 7.5 MW in #23057 and reduced gas puff in #23517, it was possible to have an approximate match of ELM frequencies in these two discharges, except in the time windows at the start of ICRF pulses in #23057. The measured sputtering yields at the antenna limiters and W concentrations are significantly lower with reduced O concentration. The possibilities for the reduction of the W release during ICRF with existing antennas in AUG are limited in the experiment and impose by themselves limits on the operational parameters. The use of large antenna-separatrix clearance leads to low antenna resistance and voltage stand-off issues in antennas and in transmission lines at high ICRF power. In addition, it has been observed [10] that at large clearance, parallel near-fields are less localized at the antenna and sputtering on remote structures connected to antennas along magnetic field lines becomes more pronounced. During ICRF, the use of high gas puff rates ($> 5 \times 10^{21} s^{-1}$ from midplane) is required to achieve a positive effect on W concentration. This usually restricts the discharges at high-confinement regimes. The experiments before the boronizations (at high O concentrations) have shown that H-mode with pure ICRF heating could only be achieved at high gas puff, high clearance, type III ELM regime, with P_{rad}/P_{ICRF} ratio of 85% and higher. With reduced O content, long after the boronizations, type I ELMy H-modes with moderate or high gas puff were achievable with P_{rad}/P_{ICRF} as low as 60% and very similar to the phases with NBI heating only. However the high-confinement regimes were still problematic with ICRF due to the rise of radiation.

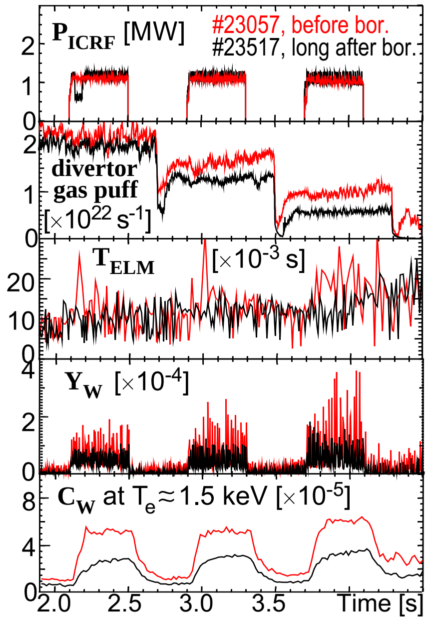

FIG. 4: Shot comparison before and long after boronization. Each shot has different levels of gas puff.

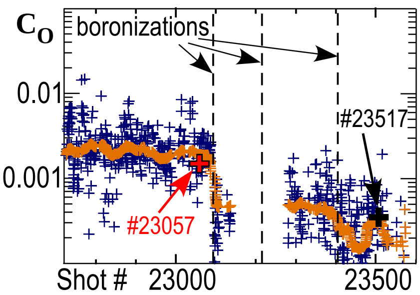

FIG. 5: O concentration evolution. Orange symbols show time-averaged behaviour.

It is therefore important to consider the second approach on reducing the W release during ICRF, namely by designing an improved antenna. For this, one needs to understand the mechanisms involved in creating the antenna near-fields and establish a relation between the experiment and calculations. The validation of the near-field calculations in the experiment allows to design antennas with reduced parallel near-fields using numerical codes.

4. Parallel near-fields of antenna

Until recently, it was usually considered that the parallel component of antenna near-fields originates from the RF magnetic flux created solely by antenna straps. In particular, the corners of a double-strap antenna where magnetic field lines pass only one out of two $(0, \pi)$ phased straps

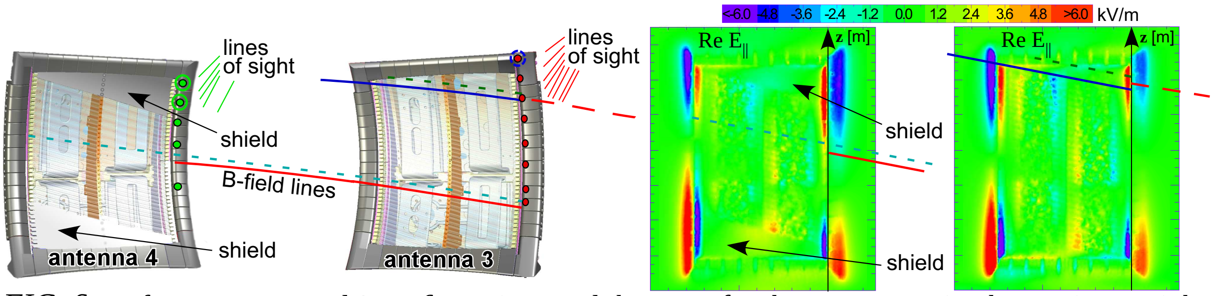

FIG. 6: Left: Antenna 4 and 3 configurations and the setup for the spectroscopic observations. Right: HFSS calculations of $E_{||}$ for 1 MW per antenna at the plane 10 mm in front of FS, at 11^o inclined magnetic field for antenna 4 and 3.

had been considered as an important contributor to $V_{||}$. However this concept cannot describe some empirical findings, for example the fact that the alignment of the Faraday Screen (FS) angle with the magnetic field angle is not crucial for the impurity production by ICRF. Recent studies which include both theoretical calculations with 3-D finite elements codes (first with ICANT [11], then with HFSS code [10]) and experimental studies (Langmuir probes [12]), have shown that all current-carrying structures surrounding the antenna, and in particular the antenna box, can produce a large contribution to $V_{||}$. The calculations have also shown that the FS effectively screens $V_{||}$ inside the antenna box, but has a little effect on the box contribution.

4.1. Experimental setup and calculations

In order to assess the validity of the calculations, it was decided to make the antenna 4 modifications shown in Fig. 6 on the left side. The installed corner shields screen the regions where the contributions from the antenna straps are not compensated. Assuming the earlier used picture of the $E_{||}$-fields based on RF magnetic flux of antenna straps is correct, the local spectroscopic measurements (Fig. 6, large green circles) should register a significant positive effect on the modified antenna. If the antenna box currents play the dominant role for the formation of $E_{||}$-fields, the same values are expected for both antennas, because the HFSS calculations (the right hand side of Fig. 6, see more details in section 5.1) have shown that the $E_{||}$ distributions (and $V_{||}$ voltages) are very similar both for the covered and the uncovered antennas.

4.2. Relation between experiment and calculations

Figure 7 shows the Y_W profiles along the vertical coordinate z of antenna 3 (uncovered) and antenna 4 (covered) in an L-mode discharge with ICRF (1 MW) only heating and a large separatrix-antenna clearance. The values for each antenna are normalized to a maximum value Y_W^{max} at each antenna to compensate for the small ($\approx$ 20%) difference between the antennas due to a toroidal asymmetry of the in-vessel structures, which causes mainly differences in connection lengths. The experimental conditions were chosen to be as close as possible to the vacuum conditions in simulations and to reduce the sensitivity of the measurements to the distance between points of observation and plasma. The latter helps to compensate for some small misalignment between the poloidal shapes of magnetic configuration of the discharge and the antenna limiter contour. The data are taken from the time windows when antenna 3 or antenna 4 is operated alone.

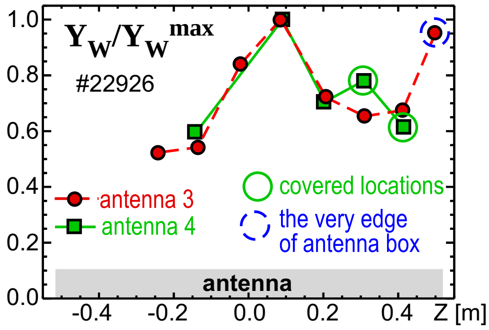

FIG. 7: Comparison between antenna 3 and antenna 4.

The spectroscopic observation points at vertical positions $Z = 0.3$ m and $Z = 0.4$ m for antenna 3 and antenna 4 show about the same Y_W/Y_W^{max} values for both antennas, although antenna 4 has the cover at these locations. The values are also a factor of 10 larger compared to the level of the sputtering yields in an ohmic discharge. This observation confirms that the covers of antenna 4 do not affect $V_{||}$ markedly. Therefore a different effect plays a more important role than the effect of uncompensated strap contributions. This effect is likely due to the box currents as indicated by the HFSS calculations. This is also confirmed by the $Z = 0.53$ m line of sight on antenna 3, which is situated on the very outer edge of the antenna and is not connected along field lines to any antenna strap. The value of Y_W/Y_W^{max} measured here is close to 1.

To establish a better relation between experiment and HFSS calculations, we compare the shape of Y_W profile along z measured when antenna 3 is operated alone (upper graph in Fig. 8) with the shape of the $V_{||}$ profile from the HFSS code, calculated by integrating $E_{||}$. The values from the experiments and the code correspond to a coupled power of 1 MW. For the reasons described below in section 5.1, we can compare only the shapes of Y_W with the shape of voltages $V_{||}$. The voltages (curves in the lower graph in Fig. 8) are calculated for different field line geometries starting at the observation locations on the antenna 3 limiter. Three main geometries can be distinguished. The colors in Fig. 8 correspond to the field lines indicated in Fig. 6 on the upper part of the antennas. The different field line geometries should be taken into account because the spectroscopic measurements integrate toroidally over a relatively broad emission region. An observation spot has a 3 cm diameter and covers both sides of the limiter. The experimental data in Fig. 8 are affected by all the field line specific $V_{||}$ contributions. Furthermore, the relative contribution of the different geometries to the measured sputtering yield can change from one vertical location to another due to changes of the field line connection length and variations of the limiter tile shape in the regions of observation. The experimental data correspond best to the RF voltages calculated for the field line geometry shown as solid blue curve. However it is difficult to make any conclusive statement on agreement between Y_W and $V_{||}$ for these conditions.

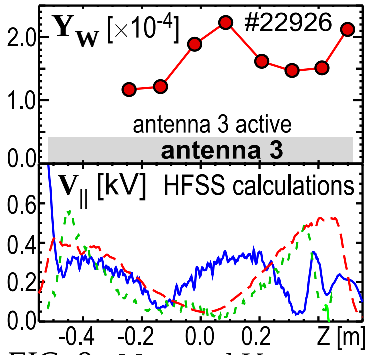

FIG. 8: Measured Y_W on active antenna 3 and calculated $V_{||}$ on the field lines.

The situation becomes easier if the right limiter of antenna 3 is used to characterize antenna 4 at the time when antenna 4 only is operated (Fig. 9). Here we also consider the field lines starting from the antenna 3 limiter. This limiter provides information on the field lines biased by antenna 4. For the magnetic configuration used, only two main field line geometries should be considered. Examples of the field lines are illustrated in Fig. 6 (lines starting on the lower part of antenna 3). The voltages calculated along the field lines of these geometries mapped onto the vertical axis z have similar profiles (lower graph of Fig. 9). The relative differences of field line connection lengths are significantly smaller than in the case for Fig. 8. Another advantage here is that the limiter area observed spectroscopically covers the whole limiter area affected by antenna 4. The shapes of the measured vertical Y_W profile and $V_{||}$ from the calculations in Fig. 9 show reasonably good agreement. This encourages the use of such calculations with HFSS to design antennas with reduced parallel near-fields.

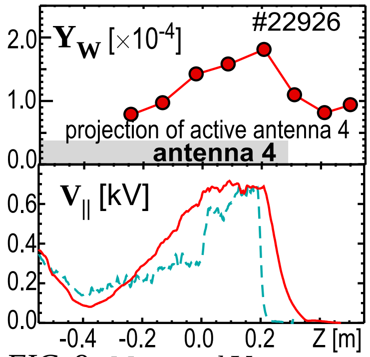

FIG. 9: Measured Y_W on non-active antenna 3 and calculated $V_{||}$ on the field lines connected to active antenna 4.

5. Use of HFSS calculations to design antenna with reduced parallel near-fields

5.1. Description of model

The HFSS calculations use a model based on planar geometry and antenna load simulated by a sea water tank. In the model an antenna is placed in a cuboid (2.27 m × 1.5 m × 0.6 m) with radiation conditions as boundaries. In the cuboid, the water tank (2.27 m × 1.5 m × 0.3 m) is placed 4 cm in front of the antenna.

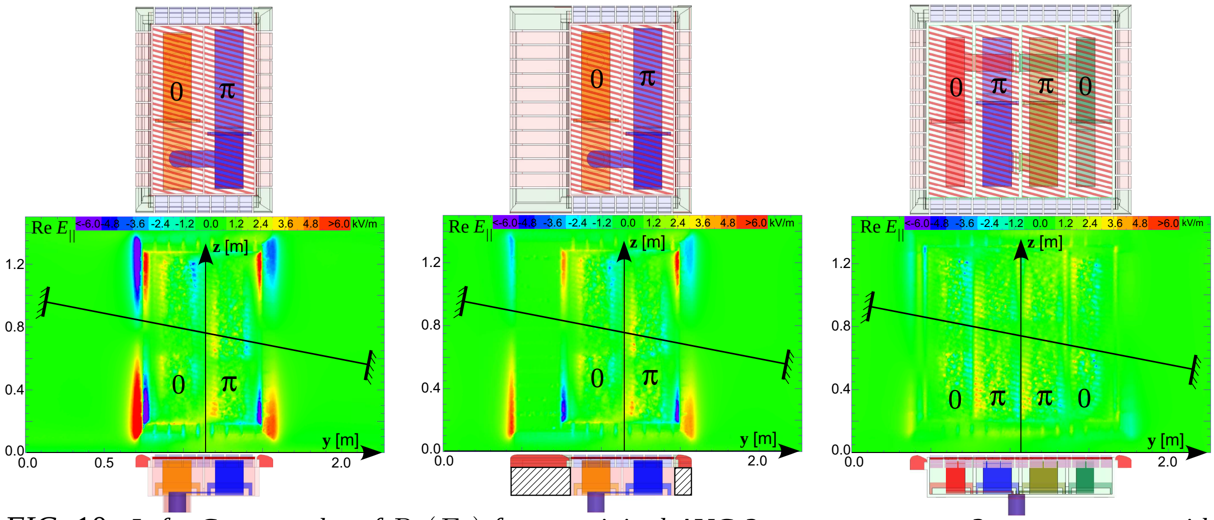

FIG. 10: *Left: Contour plot of* $Re(E_{||})$ *for an original AUG 2-strap antenna, a 2 strap antenna with broad limiter and a 4-strap optional antenna.*

The use of water instead of a plasma model leads to some restrictions on the results of calculations. The absolute values of the sheath potential drop can not be predicted accurately. In addition, the water model can not be used to model the radial distribution of the fields, because it represents the vacuum fields instead of the slow wave fields [12,13] in the plasma. Nevertheless, the model with water can be applied for the purposes described in this paper. As in section 4.2, it can be used for the comparison of the shapes (not absolute values) of poloidal profiles of the measured Y_W and the calculated $V_{||}$, both are linked to the sheath potential drop. Furthermore we use the model to find the ways to minimize the parallel near-fields, that should be independent of the model.

The output of the HFSS code consists of arrays of real and imaginary parts of the x,y,z components of the electric field at the antenna front yz plane with 2.27 m $\times$ 1.5 m dimensions. The plane is 1 cm in front of the antenna FS. The fields are re-normalized to 1 MW net power using the s_{11} antenna scattering matrix parameter. Due to relatively small asymmetry and cross-coupling between antenna straps, the error due to such normalization is below 5 %. To compare antenna concepts $V_{||} = \int E_{||} \cdot dl$ is calculated on the passing field lines which do not intersect the antenna frame. In addition, $V_{abs} = \int |E_{||}| \cdot dl$ is determined on the same field lines. A low V_{abs} represents a suppression of all $E_{||}$ fields.

5.2. Ways to reduce parallel near-fields and to improve antenna design

To reduce $V_{||}$ at or near the antenna, it is necessary to reduce $E_{||}$ fields at the antenna box. The conditions for the appearance of these fields can be described as follows. Firstly, due to the normal orientation of electric field to surfaces of a conductor, the large parallel component of the field appears at the locations where antenna frame structures, in particular limiters, are not parallel to magnetic field, i.e. at the locations where magnetic field lines intersect with the limiters. As a second condition, image currents should be present close to these locations.

To reduce $E_{||}$ fields on the box, two basic directions can be identified. The first is by extending the antenna box (or limiters) along magnetic field lines as far as possible. This shifts the locations of intersection away from the image currents. Ideally, implementation of antenna in a continuous wall which is parallel to the magnetic field would lead to a complete disappearance of $E_{||}$ on the box, because the fields would only have a perpendicular component. Applied to the original AUG antenna shown in Fig. 10 on the left side, the possible modification would include a broadening of one of the limiters (restricted due to mechanical limitations). The antenna view and calculations of $E_{||}$-fields for the antenna with the broad limiter are shown in Fig. 10 middle. One should note, that the connection of the limiters to the box shown by hatched area, is essential for the reduction of the fields.

The second direction is trying to reduce the image currents directly. This can be done by increasing the number of toroidally distributed antenna straps: for the same total launched power, the antenna with more straps has less power on the straps adjacent to the sides of antenna box and less image current on the box. In addition, for $(0\pi...\pi0)$ or $(0\pi...0\pi)$ strap phasing, the image currents of the straps adjacent to the box can be better balanced/suppressed by the outer-phase contribution of other straps. A possible 4-strap antenna utilizing this principle for $(0\pi\pi0)$ phasing is shown in Fig. 10 on the right side. Here the straps adjacent to the antenna box are made narrower than those inside the antenna, in order to have a better balance between the two counteracting (0π)-phased contributions of the image currents on the antenna box.

Comparison of $V_{||}$ and V_{abs} on the fields lines passing in front of antenna for all 3 antenna setups is shown in Fig. 11. In terms of $V_{||}$ and V_{abs} both the antenna with broad limiter and the 4-strap antenna should lead to a reduction of W sputtering. The 4-strap antenna can be further optimized by a better adjustment of the strap dimensions. Similar graphs (as in Fig. 11) were presented in [14], but for the different field lines, which cross the antenna frame and end at the right antenna limiter.

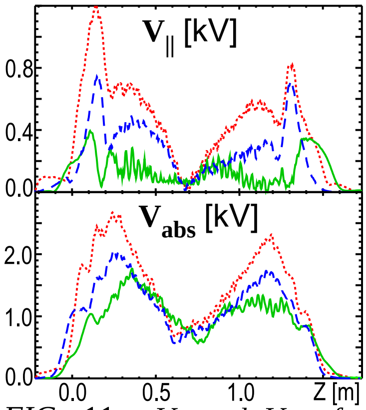

FIG. 11: $V_{||}$ and V_{abs} for original antenna (red dotted), antenna with a broad limiter (blues dashed) and 4-strap antenna (green solid).

6. Conclusions

Large antenna-separatrix and high gas puff allowed to reduce W sputtering attributed to rectified sheath effects during ICRF power application to some extent. The reduction of intrinsic impurities such as oxygen reduces the release of W significantly. In order to enlarge the operational window of efficient ICRF operation to high confinement regimes, modifications of the antenna design should be made. For this, 3D-finite elements codes, such as HFSS, can be used. Spectroscopic measurements at the antennas support the HFSS code result. The code shows the dominant role of the parasitic parallel RF fields which originate mostly from the image currents on the antenna box. This result is further confirmed by the agreement of the shapes of calculated parallel voltages with measured effective sputtering yields. Further calculations with the HFSS code suggest that a toroidal broadening of the antenna box and/or a larger number of toroidally distributed straps can reduce the parallel near-fields.

References

[1] WUKITCH, S. et al., Journal of Nuclear Materials **363-365** (2007) 491.
[2] PHILLIPS, V. et al., Plasma Phys. Control. Fusion **42** (2000) B293.
[3] KALLENBACH A. et al., Plasma Phys. Control. Fusion **47** (2005) B207.
[4] LIPSCHULTZ B. et al., Nucl. Fusion **41** (2001) 585.
[5] NEU, R et al., Plasma Phys. Control. Fusion **49**, 12B (2007) B59.
[6] DUX, R. et al., PSI-18 Conference, (2008), submitted to Journal of Nuclear Materials.
[7] DUX, R. et al., Journal of Nuclear Materials **363-365** (2007) 112.
[8] PERKINS F., Nucl. Fusion **29** 4 (1989), 583.
[9] BOBKOV, V. et al., Journal of Nuclear Materials **363-365** (2007) 122.
[10] BOBKOV, V. et al., AIP Conference Proc. AIP Press Melville NY **933** (2007) 83.
[11] COLAS L., et al., Nucl. Fusion **45** (2005) 767.
[12] COLAS L. et al., Journal of Nuclear Materials 363-365 (2007) 555.
[13] COLAS L. et al., PSI-18 Conference, (2008), submitted to Journal of Nuclear Materials.
[14] BOBKOV, V. et al., Europhysics Conference Abstracts (Proc. of the 35rd EPS Conference on Plasma Physics, Hersonissos, Crete, 2008) **32F** (2008) P.5.005.